Research Article | Vol. 26, No. 10 | 14 May 2018 | OPTICS EXPRESS 12499
Optics EXPRESS

Segmented waveguide photodetector with 90% quantum efficiency

QIANHUAN YU, KEYE SUN, QINGLONG LI, AND ANDREAS BELING*

Department of Electrical and Computer Engineering, University of Virginia, Charlottesville, VA 22904, USA
ab3pj@virginia.edu

Abstract: We demonstrate a novel InGaAsP/InP segmented waveguide photodetector based on directional couplers. By matching the imaginary parts of the propagation constants of the even and odd modes, we designed a photodetector with 6 elements, each with an absorber volume of only 19 μm^3 and a bandwidth of 15 GHz, that has an internal quantum efficiency (QE) of 90% at 1550 nm wavelength corresponding to 1.13 A/W.

OCIS codes: (230.5160) Photodetectors; (230.5170) Photodetectors.

References and links

1. D. Wake, T. P. Spooner, S. D. Perrin, and I. D. Henning, "50 GHz InGaAs edge-coupled PIN photodetector," Electron. Lett. **27**(12), 1073–1075 (1991).
2. Y. Wang, Z. Wang, Q. Yu, X. Xie, T. Posavitz, M. Jacob-Mitos, A. Ramaswamy, E. Norberg, G. Fish, and A. Beling, "High-Power Photodiodes With 65 GHz Bandwidth Heterogeneously Integrated Onto Silicon-on-Insulator Nano-Waveguides," IEEE J. Sel. Top. Quantum Electron. **24**(2), 1–6 (2017).
3. M. N. Draa, J. Bloch, D. Chen, D. C. Scott, N. Chen, S. B. Chen, X. Yu, W. S. Chang, and P. K. L. Yu, "Novel directional coupled waveguide photodiode-concept and preliminary results," Opt. Express **18**(17), 17729–17735 (2010).
4. M. S. Islam, T. Jung, T. Itoh, M. Wu, D. L. Sivco, and Y. Cho, "Velocity-matched distributed photodetectors with pin photodiodes," in *International Topical Meeting on Microwave Photonics MWP 2000*, pp. 217–220 (2000).
5. R. Nehra, C. H. Chang, A. Beling, and O. Pfister, "Photon-number-resolving segmented avalanche-photodiode detectors," arXiv:1708.09015 [physics.ins-det] (2017).
6. F. J. Effenberger and A. M. Joshi, "Ultrafast, dual-depletion region, InGaAs/InP pin detector," J. Lightwave Technol. **14**(8), 1859–1864 (1996).
7. Q. Li, K. Sun, K. Li, Q. Yu, P. Runge, W. Ebert, A. Beling, and J. C. Campbell, "High-Power Evanescently-coupled Waveguide MUTC Photodiode with >105 GHz bandwidth," J. Lightwave Technol. **35**(21), 4752–4757 (2017).
8. A. Yariv, "Coupled-mode theory for guided-wave optics," IEEE J. Quantum Electron. **9**(9), 919–933 (1973).
9. V. R. Chinni, T. C. Huang, P. K. Wai, C. R. Menyuk, and G. J. Simonis, "Crosstalk in a lossy directional coupler switch," J. Lightwave Technol. **13**(7), 1530–1535 (1995).
10. D. Marcuse, "Theory of the Directional Coupler," in *Theory of Dielectric Optical Waveguides* (1991).
11. Z. Li, H. Pan, H. Chen, A. Beling, and J. C. Campbell, "High-saturation-current modified uni-traveling-carrier photodiode with cliff layer," IEEE J. Quantum Electron. **46**(5), 626–632 (2010).

1. Introduction

High speed and high quantum efficiency photodiodes (PDs) are key devices in optical communications, sensing, and microwave photonics. To overcome the well-known bandwidth-efficiency trade-off in normal incidence PDs, side-illuminated or waveguide-photodiodes have been developed [1–3]. Waveguide PDs provide high responsivity and short carrier transit time since electrical and optical transports are not collinear. As most waveguide PDs are butt- or evanescently coupled, their responsivity primarily scales with the length of the absorption layer which can negatively impact the bandwidth and dark current in high-responsivity PDs.

In this paper, we demonstrate a monolithically integrated InP-based p-i-n segmented waveguide photodetector consisting of 6 PDs that are coupled to one waveguide. Optical coupling from the waveguide into the PD absorber and back into the waveguide was accomplished by using a vertical directional coupler design. Light that is not absorbed by the

#324614 https://doi.org/10.1364/OE.26.012499
Journal © 2018 Received 21 Feb 2018; revised 11 Apr 2018; accepted 24 Apr 2018; published 1 May 2018

Optics EXPRESS

first PD couples back into the waveguide and is absorbed in one of the following PDs. We show that the segmented photodetector can achieve near-unity quantum efficiency by using an array of 32 μm long photodiodes with an absorber thickness as small as 30 nm. Compared to the single directional coupled waveguide photodiode in ref [3], our segmented waveguide photodetector achieves higher responsivity and larger bandwidth. We believe that this type of photodetector has potential applications in travelling wave PDs with velocity-matched electrodes [4], and low dark-count photon-number resolving detectors [5] which require minimized absorber volumes and high quantum efficiency.

2. Coupled waveguide design

Figure 1(a) shows the proposed photodiode cross-section. The passive waveguide (WG1) is embedded between two lower index cladding layers and serves as the input waveguide of the photodetector. The upper cladding layer is used to separate WG1 from the second waveguide, the absorption waveguide (WG2). Adding these extra layers does not sacrifice bandwidth performance because they serve as electron drift region similar to the collection layer in dual-depletion region [6] and uni-traveling carrier PDs [7]. The light coupling process in and out of the PD can be recognized as a co-directional coupler problem as illustrated in Fig. 1(b). To ensure complete coupling, the goal is to achieve phase match, i.e. matching the propagations constants of the modes in WG1 and WG2.

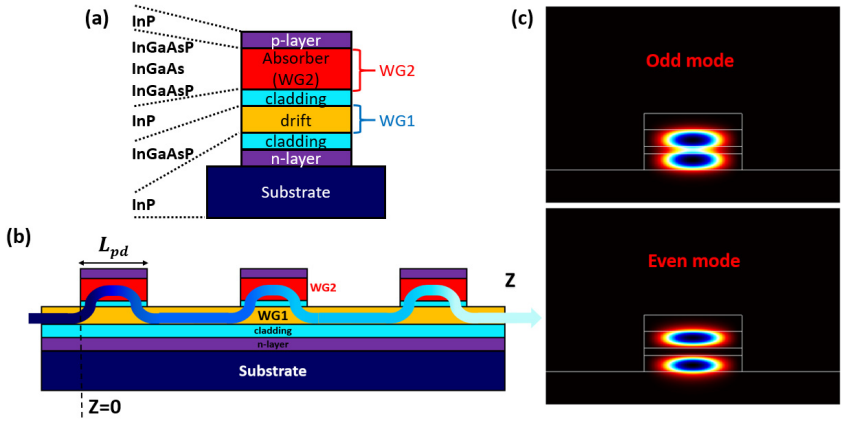

Fig. 1. (a) Cross-section of waveguide photodiode; (b) Light propagating in the segmented waveguide photodetector; (c) Intensity distribution of the anti-symmetric (odd) and symmetric (even) supermodes in the cross-section.

Figure 1(c) shows the intensity distribution of the symmetric (even) and anti-symmetric (odd) supermodes in the cross-section. Based on the theory of mode coupling [8,9], the field distribution $\varnothing_1(z)$ in WG1 and $\varnothing_2(z)$ in WG2 can be represented by adding the even mode field φ_e and the odd mode field φ_o [10]:

$$\begin{aligned}\varnothing_1(z) &= a_1\varphi_e \exp(-i\beta_e z) + a_2\varphi_o \exp(-i\beta_o z)\\ \varnothing_2(z) &= a_3\varphi_e \exp(-i\beta_e z) + a_4\varphi_o \exp(-i\beta_o z)\end{aligned} \tag{1}$$

where β_e and β_o stand for the corresponding propagation constants of these two modes and a_1, a_2, a_3 and a_4 are the coupling coefficients. When light is launched into WG1 at z = 0, it follows:

$$\varnothing_2(0) = a_3\varphi_e + a_4\varphi_o = 0 \tag{2}$$

Optics EXPRESS

In order to ensure low radiation loss, light has to completely couple back from WG2 into WG1 at the rear facet of the PD, hence it is necessary to make $\varnothing_2(l_{pd})=0$. Combining with the initial conditions (Eq. (2), the propagation constant of the odd and even modes should follow:

$$\exp\left[-i(\Delta\beta)l_{pd}\right]=1 \tag{3}$$

here △β is the difference between the even and odd mode propagation constants defined as: $\Delta\beta=\beta_e-\beta_o$. Defining $\Delta\beta_r$ and $\Delta\beta_i$ to be the real and imaginary parts of Δβ, Eq. (3) becomes:

$$\exp\left(\Delta\beta_i l_{pd}\right)\exp\left(-i\Delta\beta_r l_{pd}\right)=1. \tag{4}$$

In order to satisfy above equation, it is imperative to make $\Delta\beta_i=0$. This means, that the propagation constants of the odd and even modes have the same imaginary part. Or, in other words, only when even and odd modes attenuate at the same rate, a complete transfer of optical power between WG1 and WG2 is possible. Moreover, the PD length l_{pd} is concluded to be multiples of the beat length l, defined as:

$$l=2/\Delta\beta_r. \tag{5}$$

3. Simulation

To calculate the field distributions and propagation constants, we used the commercial software Fimmwave. In the design process we started from the simplified structure as shown in Fig. 1(a). Since changing the thickness of the cladding layer between WG1 and WG2 will change β_o and β_e simultaneously, we kept this parameter to be 220 nm to ensure sufficient field overlap between WG1 and WG2. At the same time the thickness of WG1 should be thick enough to ensure minimal field overlap with the highly doped n-contact layer and to prevent free-carrier absorption. However, a thick WG1 layer decreases the coupling efficiency from WG1 to WG2 owing to a better mode confinement. In the design we chose a 500 nm thick WG1 that can provide both, a low free-carrier absorption and a strong coupling. For moderate absorption in the first PD, the thickness of InGaAs in WG2 cannot be too thick. Sandwiching an only 30-nm thin InGaAs layer between the two InGaAsP layers results in a similar propagation constant of WG1 and WG2 with a low effective absorption coefficient in WG2.

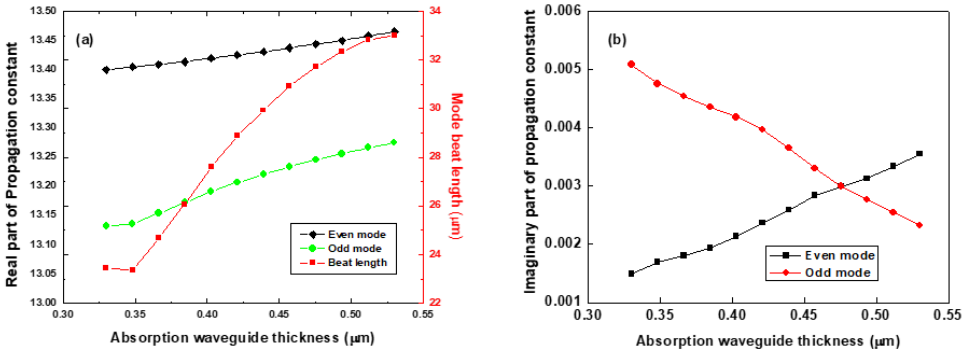

Fig. 2. (a) Real part of propagation constant and mode beat length vs. WG2 thickness. (b) Imaginary part of propagation constants vs. WG2 thickness.

Optics EXPRESS

After adopting two InGaAsP layers sandwiching a 30 nm InGaAs layer as WG2, the relationships between real part of the propagation constants (β_r) and thickness of WG2 are shown in Fig. 2(a). Here, the WG2 thickness is the total thickness of the InGaAs absorption layer and the InGaAsP layers. The β_r of the odd and even mode are both linear with the thickness of WG2. Using Eq. (5), the beat length determined by the difference of the even and odd modes' propagation constants is also shown in Fig. 2(a). The beat lengths range from 23 μm to 33 μm when the thickness of WG2 changes from 0.3 μm to 0.55 μm. In order to ensure that light couples back from WG2 to WG1, the PD length can only be an integral multiple length of the beat length. For the 30 nm thick InGaAs layer being sandwiched by two 220 nm thick InGaAsP layers, each segmented PD element should be around 30 μm. Figure 2(b) shows the simulated imaginary parts of the propagation constants (β_i) of the odd and even modes. We found that β_i of the even mode increases with WG2 thickness while the odd mode behaves vice versa. When the thickness of WG2 is 470 nm, both modes exhibit the same β_i , i.e Eq. (4) is satisfied. According to Fig. 2(a), the beat length is 32 μm in this situation.

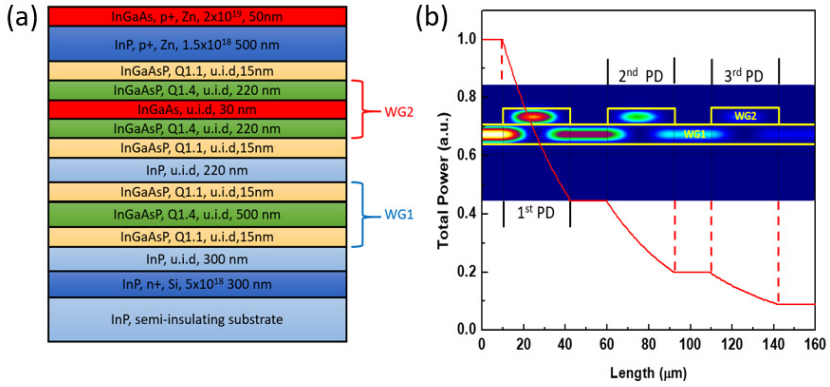

Fig. 3. (a) Epitaxial layer structure for segmented waveguide photodetector. (b) Simulation of the total power in the segmented waveguide photodetector with 3 PDs and a width of 20 μm.

Figure. 3(a) shows the complete epitaxial layer structure of the segmented waveguide photodetector that was grown on InP substrate by metal organic chemical vapor deposition. The 300 nm thick Si-doped InP layer serves as the n-type contact layer followed by an intrinsic 300 nm thick InP layer as the lower cladding. We used a 500 nm thick intrinsic InGaAsP layer as WG1 and a 220 nm thick intrinsic InP cladding layer to separate WG1 and WG2. Two InGaAsP layers sandwich the 30 nm thick InGaAs absorption layer to form WG2. The p-type contact layer is composed of a 500 nm thick highly doped InP and a 50 nm thick top InGaAs layer. We used InGaAsP Q1.1 layers to reduce the band-discontinuities at the heterojunction interfaces between the InP and InGaAsP Q1.4 layers [11]. To ensure that only the fundamental mode propagates in the passive waveguide regions, we designed an 800 μm-long tapered input waveguide. The waveguide width is 4 μm at the input (facet) and matches the PD width at its opposite end. Our simulations revealed that fundamental mode propagation can be maintained throughout the entire segmented waveguide photodetector. Figure 3(b) shows the simulated total power in the 20 μm-wide segmented photodetector with 3 elements. It can be seen that in each PD the light power decays exponentially. Assuming a lossless WG1, the power remains constant in the regions between PD segments. The simulation also predicts that the light couples completely back into WG1 at each PD's rear end.

Optics EXPRESS

4. Fabrication and characterization

A double mesa process was used to fabricate the PDs. To address the tight alignment tolerance between feeding waveguide and photodiode mesa, we used a process that defines both features in one step. The fabrication flow is summarized in Fig. 4. After blanket deposition of the p-metal, we patterned a SiO_2 hard mask and formed a ridge structure. The first mesa etch stopped at the InP n-contact layer to define WG1. Then, the n-metal was deposited. Next, a second hard mask was used to form WG2 and the n-mesa. By this way, we achieved that WG1 and WG2 have a uniform width. AuGe/Ni/Au and Ti/Pt/Au were used for n-metal and p-metal contacts, respectively. Photodiodes were connected to gold-plated pads through air-bridges, as shown in Fig. 5(b). Finally we cleaved the waveguide facet for input light coupling.

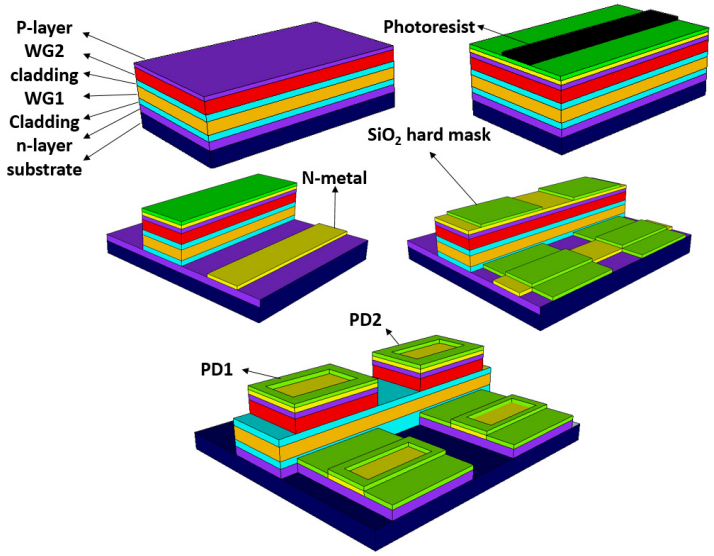

Fig. 4. Fabrication process to achieve uniform width for WG1 and WG2.

To account for uncertainties of the material refractive indices in our simulations we fabricated arrays with photodiode's lengths ranging from 20 μm to 40 μm. All PDs in an array were probed individually. We measured uniform I-V characteristics with dark currents of 1 μA at 3 V reverse voltage. We expect that the dark current can be further reduced with an appropriate side wall passivation.

The frequency responses of single PDs are shown in Fig. 5(c). The data was obtained under large-signal modulation by using an optical heterodyne setup at 1550 nm. It can be seen that a smaller PD area leads to higher bandwidth owing to the reduced capacitance. A photodiode with an active area of 300 μm^2 reached a bandwidth of 20 GHz which is higher than the bandwidth of the directional coupled waveguide photodiode in ref [3]. We estimated the transit time limited bandwidth to be 20 GHz, while the RC-limited bandwidths of the 1200 μm^2 and 300 μm^2 PDs were 34 GHz and 134 GHz, respectively. Hence, the bandwidth of the PD with an area of 300 μm^2 is mainly limited by carrier transit time effects which may explain the difference in roll-off at higher frequencies.

Optics EXPRESS

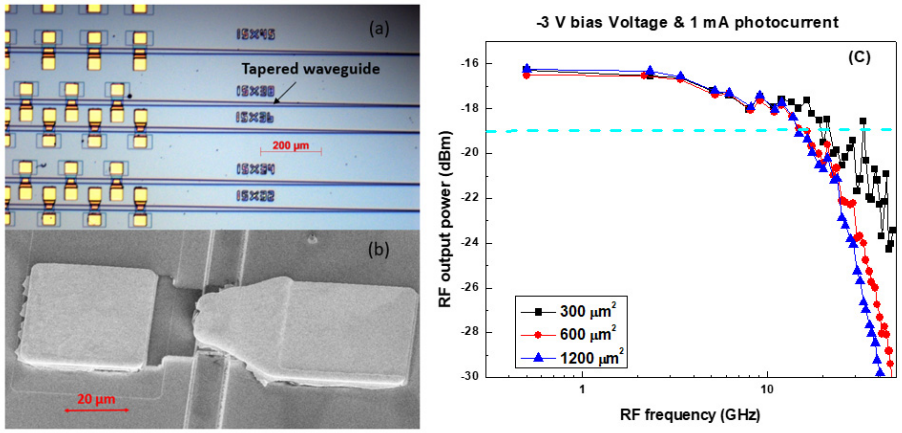

Fig. 5. (a) Microscope picture of fabricated segmented waveguide photodetector, (b) SEM pictures of PD and waveguide, (c) Bandwidth measurements of single photodiodes with different areas from the same wafer.

Using a lensed fiber with 2.5 μm spot size diameter, the quantum efficiency was measured as a function of PD length in single waveguide photodiodes. First we measured several 300 μm long single PDs to characterize the coupling loss from the fiber to the waveguide. According to our simulation, a 300 μm long PD should have an internal QE of 99%. Based on the measured external QE of (35 ± 2) %, the coupling loss from the fiber into the waveguide was calculated to be 4.5 dB. In the analysis, 1.5 dB loss are attributed to reflection at the facet since no anti-reflection coating was used. The remaining loss of 3 dB agrees with the simulated coupling loss due to mode mismatch from the fiber mode to the waveguide mode.

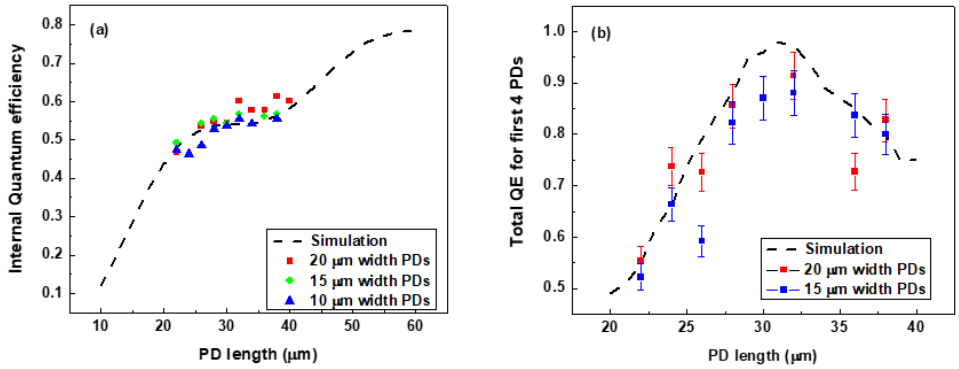

Fig. 6. (a) Measured internal QE of single PDs with different widths vs. PD length. The simulated internal QE (dashed line) showed negligible dependence on PD width. (b) Total internal QE of the segmented waveguide photodetector at a reverse bias of 3 V. The error bars come from the uncertainty in measuring the external QE of several 300 μm-long PDs that were used to determine the fiber coupling loss.

Using 4.5 dB as the coupling loss, Fig. 6(a) shows the internal QE of the first PD in segmented waveguide photodetectors with different PD lengths at a reverse bias of 3 V. The data shows that the QE only depends weakly on PD width. For a fixed width, longer PDs consistently show higher QE owing to the longer absorption length. As expected and due to mode beating phenomena, the QE scales in a non-linear fashion with PD length. This explains the relatively flat region around the calculated beat length of 30 μm in Fig. 6(a), which indicates that in this region the QE does not significantly increase as light couples back into WG1.

Optics EXPRESS

The total QE of 6 element segmented waveguide photodetectors with 15 and 20 μm widths are shown in Fig. 6(b). To determine the internal QE we added the photocurrents of the first 4 PDs in the array that were measured simultaneously, and corrected for the 4.5 dB input coupling loss. As expected from simulation, the contributions from the 5th and the 6th PDs in the array were negligible. The results show that the total internal QE increases for PD lengths larger than are 20 μm. At 32 μm PD length, the QE reaches its peak value around 90% corresponding to 1.13 A/W measured at a photocurrent of 1.7 mA. For longer PDs, the radiation loss prevails leading to a decrease in total QE. The black line in Fig. 6(b) shows the total QE by simulation. It can be seen that the measurement agrees well with the simulation within the error bars. We believe that the scattered nature of the data can be attributed to the fact that different devices came from two different chips with somewhat different facet quality. The fact that the measurement exhibits excess loss can be explained by the following reasons. First, the refractive indices that we used in the simulation may not be accurate. Together with small variations in the epitaxial layer thicknesses this may lead to a mismatch of the propagation constants of WG1 and WG2. Moreover, we did not include any waveguide loss between PD segments in our simulations.

5. Conclusion

A novel segmented waveguide photodetector based on a directional coupler design has been demonstrated. By matching the imaginary parts of the propagation constants of the even and odd modes in the design, a 6 element photodiode array achieves an internal responsivity as high as 1.13 A/W in agreement with simulations. We believe that this design finds applications in travelling wave PDs and in recently proposed photon number resolving detectors that benefit from near-unity quantum efficiency and minimized active volumes.